Journal of Materials Chemistry C

ROYAL SOCIETY OF CHEMISTRY

PAPER

View Article Online
View Journal | View Issue

Cite this: J. Mater. Chem. C, 2025, 13, 11917

The intersection of field-limited density of states and matter in radioluminescence: nanophotonic control of energy transfer†

Haley W. Jones, [ab] Yuriy Bandera[ab] and Stephen H. Foulger *[abc]

Received 16th December 2024,
Accepted 6th May 2025

DOI: 10.1039/d4tc05291a

rsc.li/materials-c

The unresolved correlation between a nanostructured environment, like a crystalline colloidal array (CCA), and the Förster resonance energy transfer (FRET) between multiple embedded emitters is a fundamental aspect of quantum light–matter interactions with implications for various high-priority applications, such as telecommunications, energy-efficient lighting, and quantum computing technologies. This highly debated topic was explored in two series (n_1 and n_2) of organic radioluminescent nanoparticles, containing a copolymerized scintillator and two organic fluorophores, that self-assembled into a liquid ordered structure, or CCA. The three copolymerized emitters exhibited two sequential transfers of energy upon X-ray irradiation, resulting in emission spanning the visible spectrum. Nanophotonic manipulation of the radioluminescence of each nanoparticle series assembled in a CCA and the energy transfer efficiency between the three emitters copolymerized within each nanoparticle series was demonstrated by positioning the partial photonic bandgap of the liquid ordered structure within the spectral regions attributed to each copolymerized emitter. Enhanced and suppressed energy transfer was exhibited in each nanoparticle series, revealing control over FRET in a radioluminescent system through strategic placement of the bandgap.

1 Introduction

The energy transfer process occurring between two quantum emitters when in nanometer proximity, known as Förster resonance energy transfer (FRET), is a vital mechanism exploited in various applications, including biosensors,[1–3] fluorescence microscopy techniques,[4] and photonic devices.[5,6] In FRET, an excited-state donor molecule nonradiatively transfers energy to a nearby ground-state acceptor molecule, typically referred to as a donor/acceptor FRET pair. FRET between quantum emitters can be manipulated through strategic engineering of the spectral properties of the donor and acceptor molecule or by adjusting the orientation of their dipole moments relative to each other.[7,8] Given the direct influence on the performance and efficiency of devices such as lasers, light-emitting diodes (LEDs), and quantum computing elements, which capitalize on the unique characteristics of confined structured environments, nanophotonic control over FRET by embedding donor and acceptor molecules within a structured environment remains a highly debated topic within the domain of quantum light–matter interactions.[9–21]

Nanophotonics plays a key role in the ongoing second quantum revolution by providing innovative ways to control and manipulate quantum states of matter at the nanoscale.[22] The manipulation of radiative decay, or spontaneous photon emission, of an emitter by a nanostructured environment, such as a photonic crystal, has been well-demonstrated in the literature.[23,24] However, studies aimed at characterizing the impact of such environments on the nonradiative interactions between emitters have faced significant challenges, contributing to the unresolved nature of this phenomenon. These challenges include manipulating photonic conditions while preserving the chemical and geometric aspects of the donor and acceptor molecules as well as selecting a precisely comparable reference to quantify photonic effects. Pioneering work by Andrew and Barnes revealed a linear relationship between the local density of optical states (LDOS) experienced by an emitter embedded within a confined structured environment and the rate of energy transfer between donor and acceptor molecules.[9] Subsequent theoretical[10] and experimental[11–13] studies were reported in the literature supporting this relationship. However, contradictory evidence has also been reported, suggesting a quadratic dependence of FRET on the LDOS[14] or no dependence at all.[17,19–21]

[a] Center for Optical Materials Science and Engineering Technologies (COMSET), Clemson University, Anderson, SC, 29625, USA. E-mail: foulger@clemson.edu
[b] Department of Materials Science and Engineering, Clemson University, Clemson, SC, 29634, USA
[c] Department of Bioengineering, Clemson University, Clemson, SC, 29634, USA

† Electronic supplementary information (ESI) available. See DOI: https://doi.org/10.1039/d4tc05291a

Photonic crystals are frequently utilized to manipulate the optical properties of embedded emitters through the photonic bandgap effect.[25–27] The inherent photonic bandgap of a photonic crystal corresponds to optical modes which are not allowed to propagate through its highly-ordered structure. Consequently, the LDOS of an embedded emitter is considerably reduced at the photonic bandgap frequency.[28] As a result, spontaneous emission at the bandgap frequency is inhibited, an effect characteristic of the weak coupling regime.[22] This work exploits colloidal photonic crystals, known as crystalline colloidal arrays, composed of electrostatically-charged nanoparticles that spontaneously self-assemble into a face-centered cubic (FCC) structure.[29–31] Due to the low refractive index contrast between the colloidal nanoparticles and liquid medium of a CCA, a CCA exhibits a partial photonic bandgap (*i.e.*, stop-band) in the visible regime.[32] CCAs are exploited in this work for their dynamic stop-band position, often referred to as the rejection wavelength (λ_{rw}), which can be shifted across the full visible spectrum by diluting the colloid.[33] Colloidal photonic crystals have been extensively exploited in various photoluminescent and optoelectronic material applications[34,35] and have proven valuable for investigations of light–matter interactions in nanostructured environments.[36–41] Importantly, the nanostructured environment of a sterically-packed colloidal crystal has been suggested to enhance nonradiative decay mechanisms, such as intersystem crossing, by the photonic bandgap effect.[41] However, investigations of radioluminescent CCAs remain limited.[42–44] It is important to note that, while the current work is limited to the weak coupling regime, further engineering of the photonic environment, such as incorporating high-Q cavities, could enable access to the strong coupling regime, where hybrid light–matter states emerge.[22] Exploring this transition presents exciting opportunities for future studies in coherent light–matter interactions;[22] however, such phenomena are beyond the scope of this work.

In the efforts to explore the unresolved dependence of FRET on the LDOS and expand upon this phenomenon in a radioluminescent system, two nanoparticle series (n_1 and n_2) were synthesized, where each series contained a copolymerized scintillator and two fluorophores. Notably, n_2 was synthesized using 100 times less emitter content than n_1. Both n_1 and n_2 spontaneously self-assemble into a CCA, allowing for dynamic control over the partial photonic bandgap position by increasing the interparticle spacing, achieved by dilution with deionized water, without chemically or geometrically altering the copolymerized emitters.[45] In both nanoparticle series, an anthracene derivative (AMMA) serves as the initial donor in the FRET system, resulting in radioluminescent nanoparticles. Anthracene is a well-known organic scintillator (*cf.* Fig. S1, ESI†) and has a scintillation efficiency comparable to that of bismuth germanium oxide (BGO), a common inorganic scintillator.[46] By utilizing an X-ray excitation source, the emitters covalently incorporated within the nanoparticles and nanoparticle building blocks of the colloidal array are collectively excited as opposed to only emitters at the surface of the nanoparticles or nanoparticles at the surface of the crystal structure. Additionally, naphthalimide and rhodamine B derivatives (NMMA and RMMA, respectively) were copolymerized within the nanoparticles, extending the emission to the red region of the visible spectrum through two sequential transfers of energy, where anthracene/naphthalimide and naphthalimide/rhodamine B are known to form FRET pairs with each other.[42–45,47] Upon nanoparticle excitation with an X-ray source, the AMMA donor transfers energy to NMMA, acting as an acceptor in the AMMA/NMMA FRET pair. Subsequently, NMMA acts as a donor and transfers energy to RMMA, acting as an acceptor in the NMMA/RMMA FRET pair. Radioluminescence (RL) measurements of n_1 and n_2 assembled into an ordered structure (OS) as the λ_{rw} was shifted across the emission of each nanoparticle series were performed, where the reference systems used to quantify photonic effects were precisely comparable in regard to nanoparticle density and emitter content.

2 Experimental

2.1 Reagents and solvents

All commercial reagents were used without further purification. Deionized (DI) water at a resistivity of 18.2 MΩ cm was acquired from a Nanopure System.

2.2 Synthesis

2.2.1 Nanoparticle series n_1 and n_2. Monodisperse n_1 and n_2 nanoparticles with three copolymerized emitters were synthesized using a previously reported[45] general emulsion polymerization procedure.[48,49] The hydrodynamic particle size of the n_1 and n_2 nanoparticles was 125 ± 8 nm and 133 ± 11 nm, respectively. The zeta potential of the n_1 and n_2 nanoparticles was −47.6 ± 1.8 mV and −49.4 ± 1.6 mV, respectively.

2.2.2 Blank polystyrene-based nanoparticles. Monodisperse "blank" polystyrene-based nanoparticles were synthesized using a previously reported[45] general emulsion polymerization procedure.[48,49] The hydrodynamic particle size and zeta potential of the nanoparticles was 132 ± 10 nm and −52.7 ± 1.5 mV, respectively.

2.3 Optical characterization

Reflectance spectra of the nanoparticles assembled in an ordered structure (OS) was collected normal to the sample surface at the [111] plane of the OS and was obtained using an Ocean Optics USB2000 fiber coupled spectrometer equipped with an Ocean Optics bifurcated fiber optic bundle (*cf.* Fig. 1E–G and 3E–G). A white light source (Ocean Optics LS-1-CAL) was attached to the input arm of the fiber optic bundle while the output arm was attached to the spectrometer. It is important to note that reflectance peaks in the blue region of the visible spectrum exhibited significant scattering (*cf.* Fig. 1E and 3E). An Amptek Inc. mini-X X-ray tube equipped with a tungsten (W) target operating at a tube voltage of 158 kV and a tube current of 25 μA was used to irradiate the colloid for RL spectral collections (*cf.* Fig. 1–3 and Fig. S1, S2, ESI†). A Horiba Jobin-Yvon MicroHR monochromator and a Horiba Jobin-Yvon Synapse cooled CCD detector was used to collect the RL spectra of the colloid.

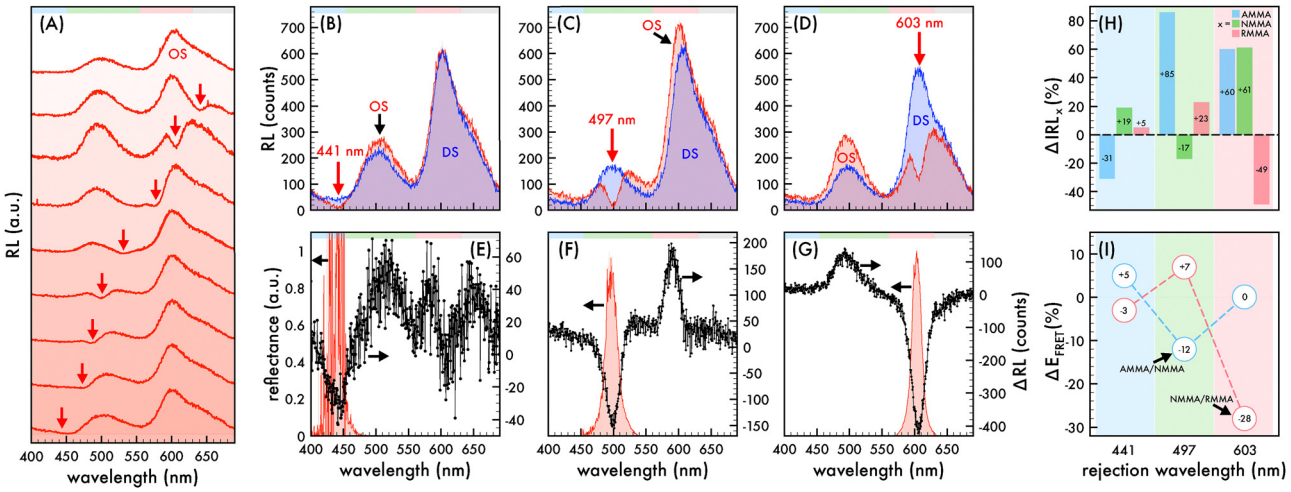

Fig. 1 Nanophotonic manipulation of n_1 radioluminescence and FRET efficiency. (A) Radioluminescence (RL) spectra of n_1 nanoparticles assembled in an ordered structure (OS) as the rejection wavelength (λ_{rw}, red arrow) was shifted across the emission spectrum. RL spectra of n_1 assembled in an OS (red) in comparison to that of corresponding disordered structures (DS, blue) as the λ_{rw} (denoted by a red arrow) was positioned to coincide with AMMA, NMMA, and RMMA emission at (B) 441 nm, (C) 497 nm, and (D) 603 nm, respectively. The difference in RL spectra (ΔRL, black dotted line) of n_1 in an OS in comparison to that of the corresponding DS as the λ_{rw} was positioned at (E) 441 nm, (F) 497 nm, and (G) 603 nm. The observed reflectance peak of each OS is presented in (E)–(G). Lightly shaded bars at the top of (A)–(G) were included as a visual aid to identify the spectral regions attributed to AMMA (blue), NMMA (green), and RMMA (red) emission. (H) Change (%) in integrated RL (ΔIRL) attributed to AMMA (blue), NMMA (green), and RMMA (red) of n_1 assembled in an OS in reference to that of the corresponding DS as the λ_{rw} was positioned at 441 nm, 497 nm, and 603 nm. (I) Difference in Förster resonance energy transfer (FRET) efficiency (ΔE_{FRET}) of the AMMA/NMMA (blue circles) and NMMA/RMMA (red circles) pairs copolymerized in n_1 when the nanoparticles were assembled in an OS in reference to that of the corresponding DS as the λ_{rw} was positioned at 441 nm, 497 nm, and 603 nm. Light shading at each λ_{rw} position is included in (H) and (I) as a visual aid to identify the overlapped emitter.

The colloid was irradiated with X-rays normal to the sample surface at the [111] plane of the OS. The RL of the colloid in the forward direction (*i.e.*, along the X-ray propagation axis) was redirected by an aluminum mirror (Thor Labs PF20-03-G01) aligned such that the transmitted light was reflected by 90 degrees into the CCD detector and the signal was collected on a grating with 600 line per mm and a blaze of 500 nm. This geometry allowed for the collection of RL spectra without placing the detector directly behind the sample, minimizing direct X-ray exposure to the detector. The exposure time and detector slit width for all samples was 30 seconds and 1 mm, respectively, unless otherwise noted. RL spectra were collected without correcting for the wavelength-dependent sensitivity of the CCD detector. Photographs of the OS were obtained with a Canon Rebel Ti1 camera (*cf.* Fig. 2D and E).

3 Results and discussion

Two series of radioluminescent polystyrene-based nanoparticles (n_1 and n_2) were synthesized by a general emulsion polymerization procedure with copolymerized derivatives of anthracene, naphthalimide, and rhodamine B (AMMA, NMMA, and RMMA, respectively) described elsewhere.[45] The n_2 nanoparticles were synthesized with 100× less emitter content than utilized in the synthesis of n_1 such that trends observed in the n_1 nanoparticles could be corroborated in nanoparticles with less emitter content. The photophysical properties of the individual emitters, confirmation of their incorporation within the n_1 and n_2 nanoparticles, and characterization of the n_1 and n_2 nanoparticles are reported elsewhere.[45] Briefly, AMMA was incorporated as the initial donor in the triple-emitter nanoparticles, where the AMMA scintillator exhibits blue emission upon X-ray excitation. When the AMMA donor is within close proximity to the NMMA acceptor, the excited-state AMMA donor nonradiatively transfers energy to the ground-state NMMA acceptor. Subsequently, the NMMA emitter acts as a donor when in close proximity to the RMMA acceptor, where the excited-state NMMA donor nonradiatively transfers energy to the ground-state RMMA acceptor. In this way, two sequential energy transfers occur within the n_1 and n_2 nanoparticles upon X-ray excitation (*cf.* Fig. S2, ESI†), where the AMMA/NMMA pair and NMMA/RMMA pair are known to exhibit FRET.[42–44] The synthesized n_1 and n_2 nanoparticles are monodisperse and colloidal stable such that they spontaneously self-assembled into a CCA.[45]

3.1 Nanophotonic manipulation of radioluminescence and X-ray-induced FRET efficiency

Manipulation of the radioluminescent spectral properties of the n_1 and n_2 nanoparticles assembled in a liquid ordered structure (OS) by the photonic bandgap effect compared to that of a precisely comparable disordered structure (DS) is presented in Fig. 1 and 3, respectively. It should be noted that all RL spectra of n_1 assembled in an OS was acquired using a small amount of n_1 nanoparticles (1.36% (v/v)) in a polystyrene-based CCA containing no copolymerized emitters due to the large quantity of emitters in the nanoparticles. As described elsewhere,[45] the size and stability of the n_1 nanoparticles and polystyrene-based nanoparticles with no copolymerized emitters were similar such

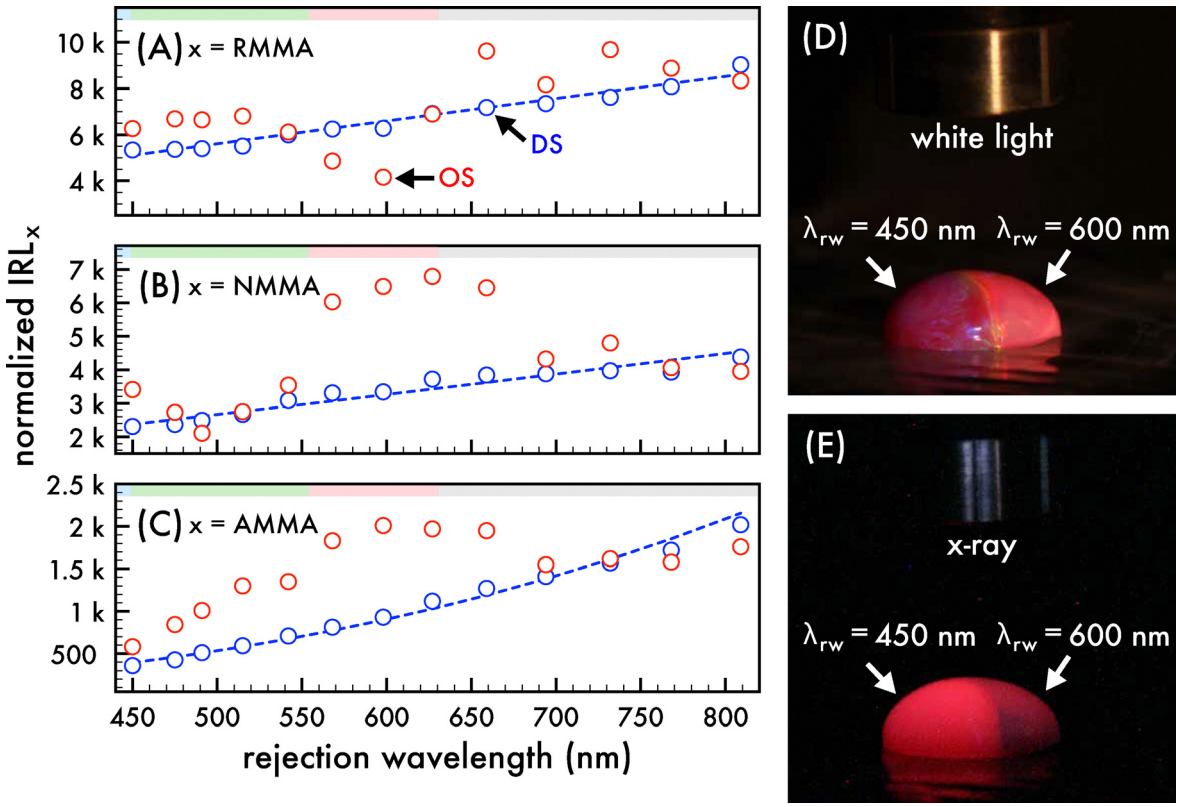

Fig. 2 Comparison of the integrated radioluminescence of n_1 assembled in an ordered structure and corresponding disordered structure with dilution. Integrated radioluminescence (IRL) normalized by the concentration of nanoparticles in each dilution of the n_1 ordered structure (OS, red circles) and disordered structure (DS, blue circles) emission attributed to (A) RMMA, (B) NMMA, and (C) AMMA as the rejection wavelength (λ_{rw}) of the OS was shifted through the visible spectrum. Lightly shaded bars at the top of (A)–(C) were included as a visual aid to identify the spectral regions attributed to AMMA (blue), NMMA (green), and RMMA (red) emission. As an aid to the eye, a trendline for the DS IRL (blue dashed line) is included in (A)–(C). Photographs of the n_1 OS under (D) white light and (E) X-ray exposure, where the λ_{rw} of the left and right half of the OS droplet is indicated.

that it was assumed that there was no preferential ordering of the particles when mixed and, thus, the placement of n_1 nanoparticles within the OS lattice was determined by the respective volume fraction (1.36%). At this volume fraction, the likelihood that two n_1 nanoparticles were located next to each other in the OS was 1 in 5405. Additionally, it should be noted that all RL spectra was obtained at the (111) face of the liquid n_1 and n_2 OS due to the alignment of the (111) face of the FCC crystal to the wall of a cuvette.[50,51] Thus, the observed λ_{rw} of the OS can be ascribed to the {111} partial photonic bandgap and the interplanar spacing (d_{111}), lattice parameter (a), and nearest neighbor spacing (a_{nn}) could be estimated and is reported elsewhere.[45]

A tungsten (W) X-ray source operating at a tube voltage and current of 25 kV and 158 μA, respectively, was utilized for all RL spectral collections. Both the n_1 and n_2 OS exhibited emission attributed to AMMA, NMMA, and RMMA when excited with an X-ray source (*cf.* Fig. 1 and 3), where the RL spectral properties of n_1 and n_2 were similar to their respective PL spectral properties described elsewhere.[45] In both n_1 and n_2, very minor emission attributed to AMMA was observed at *ca.* 405 nm and 425 nm. The maximum emission of n_1 was at 602 nm and attributed to RMMA accompanied by a smaller peak at 500 nm attributed to NMMA. The maximum emission of n_2 was at 510 nm and attributed to NMMA accompanied by a smaller peak at 590 nm attributed to RMMA. Additionally, there was a shoulder at *ca.* 650 nm in the RL spectra of n_1 and n_2 attributed to the polystyrene host polymer (*cf.* Fig. S3, ESI†) that overlapped the emission attributed to RMMA. Fig. 1A and 3A present the radioluminescent spectral characteristics of n_1 and n_2 nanoparticles assembled in an OS as the partial photonic bandgap, or observed λ_{rw} (indicated by a red arrow), was shifted through the emission of each respective OS by increasing the interparticle spacing of the OS through dilution with deionized water. Similar to observations in the photoluminescence of the n_1 and n_2 OSs,[45] suppressed emission was detected where the λ_{rw} overlapped the emission of the n_1 and n_2 OS. The RL of the n_1 and n_2 nanoparticles assembled in an OS was compared to a reference disordered structure (DS) at the same nanoparticle density and emitter content for each λ_{rw} position. A precisely comparable DS was fabricated for each λ_{rw} position of the n_1 and n_2 OS by disrupting the long-range order of the self-assembled nanoparticles. This was achieved by adding a small amount of ionic impurity to the OS, which disintegrated the crystal structure while maintaining the concentration of nanoparticles and emitter content for a controlled investigation of purely photonic effects. By comparing the difference in RL (ΔRL) of the n_1 OS compared to the DS at each λ_{rw} condition, a −71%, −77%, and −71% decrease in n_1 OS emission at the λ_{rw}

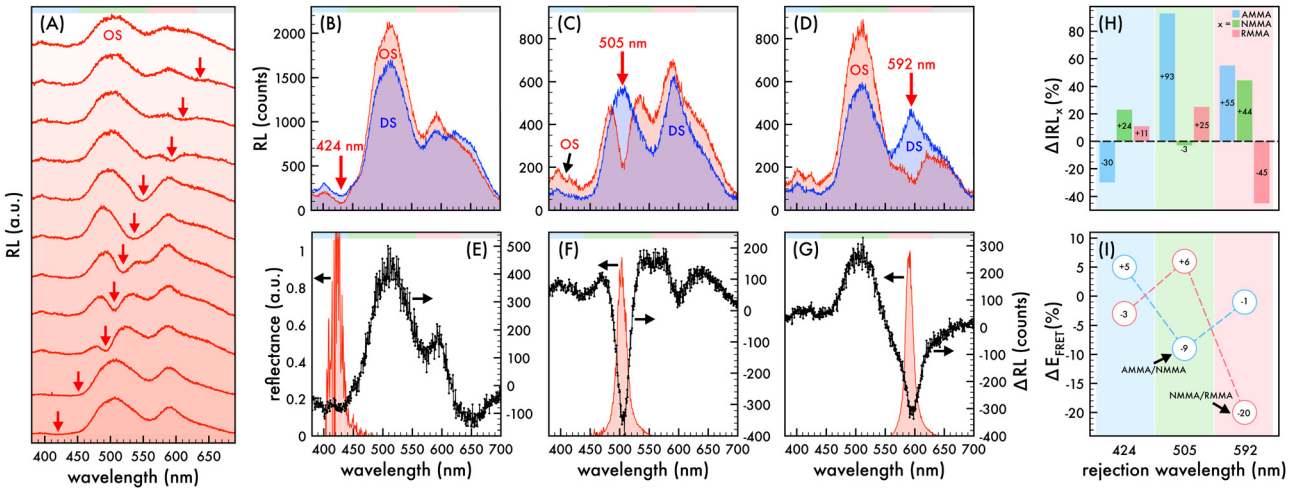

Fig. 3 Nanophotonic manipulation of n_2 radioluminescence and FRET efficiency. (A) Radioluminescence (RL) spectra of n_2 nanoparticles assembled in an ordered structure (OS) as the rejection wavelength (λ_{rw}, red arrow) was shifted across the emission spectrum. RL spectra of n_2 assembled in an OS (red) in comparison to that of corresponding disordered structures (DS, blue) as the λ_{rw} (denoted by a red arrow) was positioned to coincide with AMMA, NMMA, and RMMA emission at (B) 424 nm, (C) 505 nm, and (D) 592 nm, respectively. The difference in RL spectra (ΔRL, black dotted line) of n_2 in an OS in comparison to that of the corresponding DS as the λ_{rw} was positioned at (E) 424 nm, (F) 505 nm, and (G) 592 nm. The observed reflectance peak of each OS is presented in (E)–(G). Lightly shaded bars at the top of (A)–(G) were included as a visual aid to identify the spectral regions attributed to AMMA (blue), NMMA (green), and RMMA (red) emission. (H) Change (%) in integrated RL (ΔIRL) attributed to AMMA (blue), NMMA (green), and RMMA (red) of n_2 assembled in an OS in reference to that of the corresponding DS as the λ_{rw} was positioned at 424 nm, 505 nm, and 592 nm. (I) Difference in Förster resonance energy transfer (FRET) efficiency (ΔE_{FRET}) of the AMMA/NMMA (blue circles) and NMMA/RMMA (red circles) pairs copolymerized in n_2 when the nanoparticles were assembled in an OS in reference to that of the corresponding DS as the λ_{rw} was positioned at 424 nm, 505 nm, and 592 nm. Light shading at each λ_{rw} position is included in (H) and (I) as a visual aid to identify the overlapped emitter.

integrated over the spectral regime corresponding to the full width at half maximum (FWHM) of the reflectance peak was revealed when the λ_{rw} was at 441 nm, 497 nm, and 603 nm, respectively (*cf.* Fig. 1B–G). Through a similar comparison, a −40%, −54%, and −65% decrease in n_2 OS emission at the λ_{rw} integrated over the spectral regime corresponding to the FWHM of the reflectance peak was detected when the λ_{rw} of the n_2 OS was at 424 nm, 505 nm, and 592 nm, respectively (*cf.* Fig. 3B–G). The suppressed emission at the λ_{rw} coincidence is indicative of the reduced LDOS at the λ_{rw} and a manifestation of the Purcell effect.[52] The Purcell effect describes the enhancement or suppression of spontaneous emission of an emitter as a result of the interaction between the emitter and its surrounding environment. When the partial photonic bandgap reduces the probability of the emitter to decay by radiative processes, such as photon emission, it is hypothesized that the likelihood of the emitter to decay by nonradiative processes, such as FRET, is enhanced. Investigations of the photoluminescence of the n_1 and n_2 OS supporting this hypothesis have been previously reported;[45] however, the RL of the n_1 and n_2 OS has not been explored. Fig. 1H and 3H present the change in integrated RL (ΔIRL) attributed to each copolymerized emitter in the n_1 and n_2 OS compared to that of the precisely comparable DS, respectively, as the λ_{rw} of each OS was shifted through the emission spectrum. Additionally, the FRET efficiency (E_{FRET}) of each donor/acceptor pair could be estimated by eqn (1) (*cf.* Tables S1–S4, ESI†), where the donor and acceptor emission intensity is denoted as I_D and I_A, respectively. The change in E_{FRET} (ΔE_{FRET}) as the λ_{rw} was shifted to overlap each emitter in the n_1 and n_2 OS is presented in Fig. 1I and 3I, respectively.

$$E_{FRET} = 1 - \frac{I_D}{I_D + I_A} \quad (1)$$

3.1.1 Nanoparticle series n_1. When the λ_{rw} of the n_1 OS overlapped the AMMA donor emission at 441 nm (*cf.* Fig. 1B and E), the total RL of the OS increased by +9%. While the overall emission attributed to the AMMA donor decreased by −31% due to the decreased LDOS at the λ_{rw}, the emission attributed to the NMMA acceptor/donor and RMMA acceptor increased by +19% and +5%, respectively. The increase in NMMA and RMMA emission is attributed to the enhanced probability of the AMMA donor to decay nonradiatively and increased amount of energy transferred to NMMA and, subsequently, to RMMA. When the donor emission was suppressed, a +5% increase in FRET efficiency of the AMMA/NMMA pair was observed. However, a −3% decrease in FRET efficiency of the NMMA/RMMA pair was observed due to the greater enhancement of NMMA emission compared to that of RMMA. When the λ_{rw} of the n_1 OS overlapped the NMMA acceptor/donor emission at 497 nm (*cf.* Fig. 1C and F), the total RL of the OS increased by +14%. While the overall emission attributed to the NMMA acceptor/donor decreased by −17% due to the decreased LDOS at the λ_{rw}, the emission attributed to the AMMA donor and RMMA acceptor increased by +85% and +23%, respectively. The increase in AMMA emission is attributed to the suppressed probability of the NMMA acceptor to emit a photon, resulting in a decreased amount of energy transferred from AMMA to NMMA. The increase in RMMA emission is attributed to the

enhanced probability of the NMMA donor to decay nonradiatively and increased amount of energy transferred to RMMA. When NMMA emission was suppressed, a −12% decrease in FRET efficiency of the AMMA/NMMA pair was observed due to the suppressed energy transfer. Conversely, a +7% increase in FRET efficiency of the NMMA/RMMA pair was observed due to the enhanced energy transfer. Lastly, when the λ_{rw} of the n_1 OS overlapped the RMMA acceptor emission at 603 nm (*cf.* Fig. 1D and G), the total RL of the OS decreased by −12%. While the overall emission attributed to the RMMA acceptor decreased by −49% due to the decreased LDOS at the λ_{rw}, the emission attributed to the NMMA acceptor/donor and AMMA donor increased by +61% and +60%, respectively. The increase in NMMA emission is attributed to the suppressed probability of the RMMA acceptor to emit a photon, resulting in a decreased amount of energy transferred from NMMA to RMMA. The increase in AMMA emission is attributed to the suppressed amount of energy that AMMA is able to transfer to NMMA when NMMA is unable to subsequently transfer this energy to RMMA. When RMMA emission was suppressed, no change in the FRET efficiency of the AMMA/NMMA pair was observed due to the approximately proportional enhancement of AMMA and NMMA emission. However, the largest decrease of −28% was observed in FRET efficiency of the NMMA/RMMA pair due to the suppressed energy transfer.

To confirm that the trends observed in the n_1 nanoparticles were due to photonic effects, the integrated RL attributed to each emitter in the n_1 OS was compared to that of corresponding DSs as the λ_{rw} of the OS was shifted from *ca.* 451 nm to 810 nm (*cf.* Fig. 2A–C). For this study, a n_1 DS was fabricated at the same initial particle density of the n_1 OS and each structure was diluted by deionized water in similar quantities such that the nanoparticle densities remained closely matched. The integrated RL presented in Fig. 2 was normalized by the number of nanoparticles in the colloid at each dilution. It is important to note that both the sampled area and volume of the structures remained invariant through the dilution. Thus, as the structures were diluted, a decreased number of nanoparticles were optically sampled. This resulted in a decreased amount of scattering and increased amount of light able to pass through the colloid at each dilution. While the integrated RL of each emitter in the DS exhibited a relatively steady positive increment with increasing dilution, the integrated RL attributed to each emitter in the OS did not exhibit this same trend. Instead the OS exhibited fluctuations of increased or decreased emission, depending on the position of the partial photonic bandgap. It is important to note that the integrated RL of AMMA did not exhibit a drop below the DS trendline at the initial λ_{rw} condition owing to the λ_{rw} located at 451 nm, which is slightly red-shifted with respect to the spectral region attributed to AMMA emission and yielded a slightly enhanced AMMA emission. Nonetheless, regions of decreased integrated RL compared to that of the DS were observed for the NMMA and RMMA emitters as the λ_{rw} was shifted to overlap their respective regimes of emission. Additionally, regions of enhanced integrated RL compared to that of the DS were observed for all three emitters when the λ_{rw} overlapped their respective FRET pair. Specifically, when the λ_{rw} was near the emission attributed to the donor AMMA, enhanced emission attributed to the acceptor/donor NMMA and acceptor RMMA was evident. As the λ_{rw} was red-shifted to overlap the emission of acceptor/donor NMMA, increased emission attributed to the donor AMMA and acceptor RMMA was observed. By further shifting the λ_{rw} to overlap the emission attributed to the acceptor RMMA, increased emission attributed to the donor AMMA and acceptor/donor NMMA was detected. Finally, as the λ_{rw} of the OS was red-shifted past the RL spectrum of the n_1 nanoparticles at *ca.* >700 nm, the integrated RL of AMMA, NMMA, and RMMA closely matched that of the DS. The enhancement and suppression of FRET between the copolymerized emitters in the undiluted n_1 OS is presented in Fig. 2D and E, where photographs of a liquid droplet of the n_1 OS under white light and X-ray excitation are presented, respectively. The left half of the n_1 OS droplet had a λ_{rw} at 450 nm and exhibited an optically brighter output due to the enhanced total emission when excited with an X-ray source. The right half of the n_1 OS droplet had a λ_{rw} at 600 nm, resulting in an optically dimer output due to the suppressed total emission when excited with an X-ray source.

3.1.2 Nanoparticle series n_2. When the λ_{rw} of the n_2 OS overlapped the AMMA donor emission at 424 nm (*cf.* Fig. 3B and E), the total RL of the OS increased by +10%. While the overall emission attributed to the AMMA donor decreased by −30% due to the decreased LDOS at the λ_{rw}, the emission attributed to the NMMA acceptor/donor and RMMA acceptor increased by +24% and +11%, respectively. The increase in NMMA and RMMA emission is attributed to the enhanced probability of the AMMA donor to decay nonradiatively and increased amount of energy transferred to NMMA and, subsequently, to RMMA. When the donor emission was suppressed, a +5% increase in FRET efficiency of the AMMA/NMMA pair was observed. However, a −3% decrease in FRET efficiency of the NMMA/RMMA pair was observed due to the greater enhancement of NMMA emission compared to that of RMMA. When the λ_{rw} of the n_2 OS overlapped the NMMA acceptor/donor emission at 505 nm (*cf.* Fig. 3C and F), the total RL of the OS increased by +21%. While the overall emission attributed to the NMMA acceptor/donor decreased by −3% due to the decreased LDOS at the λ_{rw}, the emission attributed to the AMMA donor and RMMA acceptor increased by +93% and +25%, respectively. The increase in AMMA emission is attributed to the suppressed probability of the NMMA acceptor to emit a photon, resulting in a decreased amount of energy transferred from AMMA to NMMA. The increase in RMMA emission is attributed to the enhanced probability of the NMMA donor to decay nonradiatively and increased amount of energy transferred to RMMA. When NMMA emission was suppressed, a −9% decrease in FRET efficiency of the AMMA/NMMA pair was observed due to the suppressed energy transfer. Conversely, a +6% increase in FRET efficiency of the NMMA/RMMA pair was observed due to the enhanced energy transfer. Lastly, when the λ_{rw} of the n_2 OS overlapped the RMMA acceptor emission at 592 nm (*cf.* Fig. 3D and G), the total RL of the OS increased by +9%. While the overall emission attributed to the RMMA acceptor decreased by −45% due to the decreased LDOS at the λ_{rw}, the

emission attributed to the NMMA acceptor/donor and AMMA donor increased by +44% and +55%, respectively. The increase in NMMA emission is attributed to the suppressed probability of the RMMA acceptor to emit a photon, resulting in a decreased amount of energy transferred from NMMA to RMMA. The increase in AMMA emission is attributed to the suppressed amount of energy that AMMA is able to transfer to NMMA when NMMA is unable to subsequently transfer this energy to RMMA. When RMMA emission was suppressed, a slight decrease (−1%) in FRET efficiency of the AMMA/NMMA pair was observed due to the slightly greater enhancement of AMMA emission compared to that of NMMA. However, the largest decrease of −20% was observed in the FRET efficiency of the NMMA/RMMA pair due to the suppressed energy transfer.

Corroborating the results observed in investigations of the photoluminescence of the n_1 and n_2 OSs,[45] the RL of the FRET acceptor in n_1 and n_2 was enhanced when that of the corresponding FRET donor was suppressed by the partial photonic bandgap. In the opposite case, the RL of the FRET donor n_1 and n_2 was enhanced when that of the corresponding FRET acceptor was suppressed by the partial photonic bandgap.

4 Conclusions

These results support and expand upon previously reported evidence that the nonradiative transfer of energy between multiple emitters can be manipulated and controlled by the photonic bandgap effect. Similar to observations of the photoluminescence of the nanoparticle series investigated in this work, modulations of the efficiency and direction of the X-ray-induced FRET between two FRET pairs (AMMA/NMMA and NMMA/RMMA) copolymerized within two radioluminescent nanoparticle series (n_1 and n_2) assembled into CCAs were demonstrated. The efficiency of the X-ray-induced FRET between a donor/acceptor pair could be enhanced by overlapping the donor emission with the partial photonic bandgap. However, by overlapping the acceptor emission with the partial photonic bandgap, the efficiency of X-ray-induced FRET between a donor/acceptor pair could be suppressed. These results support the connection between the LDOS and FRET between emitters and present evidence that this phenomenon can be leveraged in radioluminescent systems to methodically manipulate the quantum interactions between multiple emitters. To the best of our knowledge, this is the first example of FRET manipulation by the photonic bandgap effect in a radioluminescent CCA.

Author contributions

H. J. contributed to the conceptualization, methodology, investigation, data curation, visualization, writing – original draft, and writing – review & editing. Y. B. contributed to the resources and methodology. S. F. contributed to the conceptualization, methodology, data curation, visualization, writing – original draft, and writing – review & editing.

Data availability

The data supporting this article have been included as part of the ESI.†

Conflicts of interest

There are no conflicts to declare.

Acknowledgements

The authors thank the Gregg-Graniteville Foundation and the National Science Foundation (OIA-1632881) for financial support.

References

1 I. L. Medintz, A. R. Clapp, H. Mattoussi, E. R. Goldman, B. Fisher and J. M. Mauro, *Nat. Mater.*, 2003, **2**, 630–638.
2 R. D. Fritz, M. Letzelter, A. Reimann, K. Martin, L. Fusco, L. Ritsma, B. Ponsioen, E. Fluri, S. Schulte-Merker and J. van Rheenen, *Sci. Signaling*, 2013, **6**, rs12.
3 G. C. H. Mo, C. Posner, E. A. Rodriguez, T. Sun and J. Zhang, *Nat. Commun.*, 2020, **11**, 1848.
4 E. A. Jares-Erijman and T. M. Jovin, *Nat. Biotechnol.*, 2003, **21**, 1387–1395.
5 L. Cerdán, E. Enciso, V. Martín, J. Bañuelos, I. López-Arbeloa, A. Costela and I. García-Moreno, *Nat. Photonics*, 2012, **6**, 621–626.
6 S. Buckhout-White, C. M. Spillmann, W. R. Algar, A. Khachatrian, J. S. Melinger, E. R. Goldman, M. G. Ancona and I. L. Medintz, *Nat. Commun.*, 2014, **5**, 5615.
7 T. Förster, *Ann. Phys.*, 1948, **437**, 55–75.
8 D. L. Andrews and J. Rodriguez, *J. Chem. Phys.*, 2007, **127**, 084509.
9 P. Andrew and W. L. Barnes, *Science*, 2000, **290**, 785–788.
10 H. T. Dung, L. Knoll and D. G. Welsch, *Phys. Rev. A: At., Mol., Opt. Phys.*, 2002, **65**, 043813.
11 P. Ghenuche, J. de Torres, S. B. Moparthi, V. Grigoriev and J. Wenger, *Nano Lett.*, 2014, **14**, 4707–4714.
12 D. Weeraddana, M. Premaratne, S. D. Gunapala and D. L. Andrews, *J. Chem. Phys.*, 2017, **147**, 074117.
13 S. Patra, J.-B. Claude and J. Wenger, *ACS Photonics*, 2022, **9**, 2109–2118.
14 T. Nakamura, M. Fujii, S. Miura, M. Inui and S. Hayashi, *Phys. Rev. B: Condens. Matter Mater. Phys.*, 2006, **74**, 045302.
15 B. Kolaric, K. Baert, M. Van der Auweraer, R. A. L. Vallee and K. Clays, *Chem. Mater.*, 2007, **19**, 5547–5552.
16 L. Gonzalez-Urbina, K. Baert, B. Kolaric, J. Perez-Moreno and K. Clays, *Chem. Rev.*, 2012, **112**, 2268–2285.
17 M. J. A. de Dood, J. Knoester, A. Tip and A. Polman, *Phys. Rev. B: Condens. Matter Mater. Phys.*, 2005, **71**, 115102.
18 F. T. Rabouw, S. A. den Hartog, T. Senden and A. Meijerink, *Nat. Commun.*, 2014, **5**, 3610.
19 C. Blum, N. Zijlstra, A. Lagendijk, M. Wubs, A. P. Mosk, V. Subramaniam and W. L. Vos, *Phys. Rev. Lett.*, 2012, **109**, 203601.

20 M. Wubs and W. L. Vos, *New J. Phys.*, 2016, **18**, 053037.
21 G. Rosolen, B. Maes, P. Y. Chen and Y. Sivan, *Phys. Rev. B*, 2020, **101**, 155401.
22 B. Kolaric, B. Maes, K. Clays, T. Durt and Y. Caudano, *Adv. Quantum Technol.*, 2018, **1**, 1800001.
23 K. H. Drexhage, *J. Lumin.*, 1970, **1**(2), 693–701.
24 W. L. Barnes, *J. Mod. Opt.*, 1998, **45**, 661–669.
25 T. Okubo, *Prog. Polym. Sci.*, 1993, **18**, 481–517.
26 E. Yablonovitch, *Phys. Rev. Lett.*, 1987, **58**, 2059–2062.
27 S. John, *Phys. Rev. Lett.*, 1987, **58**, 2486–2489.
28 J. D. Joannopoulos, S. G. Johnson, J. N. Winn and R. D. Meade, *Photonic Crystals: Molding the Flow of Light*, Princeton University Press, 2nd edn, 2008.
29 P. A. Hiltner, Y. S. Papir and I. M. Krieger, *J. Phys. Chem.*, 1971, **75**, 1881–1886.
30 P. A. Hiltner and I. M. Krieger, *J. Phys. Chem.*, 1969, **73**, 2386.
31 N. Clark, A. Hurd and B. Ackerson, *Nature*, 1979, **281**, 57–60.
32 P. Rundquist, P. Photinos, S. Jagannathan and S. Asher, *J. Chem. Phys.*, 1989, **91**, 4932–4941.
33 C. López, *Adv. Mater.*, 2003, **15**, 1679–1704.
34 J. R. Lawrence, Y. Ying, P. Jiang and S. H. Foulger, *Adv. Mater.*, 2006, **18**, 300–303.
35 J. R. Lawrence, G.-H. Shim, P. Jiang, M. Han, Y. Ying and S. H. Foulger, *Adv. Mater.*, 2005, **17**, 2344–2349.
36 J. Martorell and N. M. Lawandy, *Phys. Rev. Lett.*, 1990, **65**, 1877–1880.
37 B. Tong, P. John, Y. Zhu, Y. Liu, S. Wong and W. Ware, *J. Opt. Soc. Am. B*, 1993, **10**, 356–359.
38 M. Megens, J. E. G. J. Wijnhoven, A. Lagendijk and W. L. Vos, *Phys. Rev. A: At., Mol., Opt. Phys.*, 1999, **59**, 4727–4731.
39 K. Shibata, H. Kimura, A. Tsuchida and T. Okubo, *Colloid Polym. Sci.*, 2006, **285**, 127–133.
40 M. Khokhar, Priya and R. V. Nair, *Phys. Rev. A*, 2020, **102**, 013502.
41 L. González-Urbina, J. Perez-Moreno, K. Clays and B. Kolaric, *Mol. Phys.*, 2016, **114**, 2248–2252.
42 M. K. Burdette, Y. P. Bandera, G. M. Gray and S. H. Foulger, *Adv. Opt. Mater.*, 2019, **7**, 1801142.
43 M. K. Burdette, H. W. Jones, Y. Bandera and S. H. Foulger, *Opt. Mater. Express*, 2019, **9**, 1416–1429.
44 S. Mell, H. W. Jones, Y. P. Bandera and S. H. Foulger, *Langmuir*, 2022, **38**, 10089–10097.
45 H. W. Jones, Y. Bandera and S. H. Foulger, *J. Mater. Chem. C*, 2025, **13**, 1694–1703.
46 S. Kubota, T. Motobayashi, J. Ruan, T. Murakami, J. Kasagi and T. Shimizu, *IEEE Trans. Nucl. Sci.*, 1987, **34**, 438–441.
47 H. W. Jones, Y. Bandera, I. K. Foulger, I. Luzinov and S. H. Foulger, *Adv. Photonics Res.*, 2024, **5**, 2300296.
48 M. E. Woods, J. S. Dodge, I. M. Krieger and P. E. Pierce, *J. Paint Technol.*, 1968, **40**, 541.
49 Y. S. Papir, M. E. Woods and I. M. Krieger, *J. Paint Technol.*, 1970, **42**, 571–578.
50 Y. Monovoukas and A. P. Gast, *J. Colloid Interface Sci.*, 1989, **128**, 533–548.
51 Y. Monovoukas and A. P. Gast, *Phase Transitions*, 1990, **21**, 183.
52 E. Purcell, *Phys. Rev.*, 1946, **69**, 681.